

Damage assessment for buried structures against internal blast load

G.W. Ma[†], X. Huang[‡] and J.C. Li^{†‡}

School of Civil and Environmental Engineering, Nanyang Technological University,
50 Nanyang Avenue, Singapore 639798

(Received February 16, 2009, Accepted March 30, 2009)

Abstract. Damage assessment for buried structures against an internal blast is conducted by considering the soil-structure interaction. The structural element under analysis is assumed to be rigid-plastic and simply-supported at both ends. Shear failure, bending failure and combined failure modes are included based on five possible transverse velocity profiles. The maximum deflections with respect to shear and bending failure are derived respectively by employing proper failure criteria of the structural element. Pressure-Impulse diagrams to assess damage of the buried structures are subsequently developed. Comparisons have been done to evaluate the influences of the soil-structure interaction and the shear-to-bending strength ratio of the structural element. A case study for a buried reinforced concrete structure has been conducted to show the applicability of the proposed damage assessment method.

Keywords: combined failure; P-I diagram; buried structure; blast load; damage assessment.

1. Introduction

Damage assessment is a critical issue in protective structure design against blast load. Among the existing damage assessment methods, the simplified single-degree-of-freedom (SDOF) system has been widely used to analyze the structural response under blast load for a variety of structures or structural elements (Krauthammer *et al.* 1986, Li and Meng 2002a, Campidelli and Viola 2007, Fallah and Louca 2007). The SDOF system has its advantages in deriving analytically the structural response. In many cases of practical engineering, it has been used to give a preliminary assessment of structural damage induced by a blast load. However, due to its inherent limitation, the SDOF model oversimplifies the structural elements and neglects the influence of shear deformation, or it can only analyze the shear and bending response separately (Krauthammer *et al.* 1986).

In a blast event, structures at a close-in distance may experience localized transverse shear failure which deforms as a shear hinge (Symonds 1968, Jones 1989, Jones 1997). Depending on different loading rates, intensities, and material properties, the localized shear deformation can be isothermal rupture (Menkes and Opat 1973) or adiabatic shear banding failure (Kalthoff and Winkler 1987, Kalthoff 1990). Based on experimental and analytical results, researchers realized that, when the

[†] Assistant Professor, Corresponding author, E-mail: cgwma@ntu.edu.sg

[‡] Ph.D. Student, E-mail: q060022@ntu.edu.sg

^{†‡} Research Fellow, E-mail: JCLi@ntu.edu.sg

span-to-height ratio of a structural element is relatively small or when a detonation is at a close-in distance from the structure, the shear failure probably occurs. If the duration of the blast load is sufficiently short, shear failure becomes dominant and cannot be ignored.

To overcome the limitation of the SDOF model in analyzing combined failure modes, a mode approximation method for rigid-plastic structural elements has been proposed (Martin and Symonds 1966, Symonds and Chon 1979, Jones and Song 1986, Liu and Jones 1988, Li and Jones 1999, Alves and Jones 2002, Jones and Jones 2002, Li and Jones 2005a, Lellep and Torn 2005). Although the rigid-plastic model neglects the elastic deformation, the estimated deflections by the mode approximation method in most cases agree well with the final deflections observed in tests (Symonds and Chon 1979). And the pressure-impulse (P-I) diagrams derived from such model agree well with those from elastic, perfectly plastic SDOF model, especially when severe damage occurs. Lellep and Torn (2005) developed a method for investigation of rigid-plastic beams subjected to impulse load. Close-form solutions were derived for beams made of perfectly plastic material obeying the square yield condition. According to this method, the shear and bending responses can be analyzed at the same time. Ma *et al.* (2007) derived explicit forms of P-I diagrams based on the rigid-plastic beam model for structural elements subjected to a blast load.

However, the most existing works focused on damage assessment of surface structures. Very few involved in failure of underground buried structures. In fact, the complexity of soil property makes it difficult to perform structure response analysis when the soil-structure interaction is considered. It is understood the surrounding soil interacts with the buried structural element during the loading phase. The soil acts as an elastic support which absorbs part of the blast energy during an internal blast event occurred to a buried structure.

In the present study, the soil-structure interaction is simplified as a spring effect. The rigid plastic model with the mode approximation method is adopted. Pressure-impulse diagrams are subsequently developed for structural element by considering the soil-structure interactions. The results of the present study can also be applied to the scenarios when the explosion occurs nearby a retaining wall, over a foundation slab, and basement, etc. Comparison between the present study and damage assessment for surface structures is carried out to evaluate the soil-structure interaction effect. P-I diagrams of different damage levels are also plotted. To verify the continuity of different failure modes, verifications are done by checking a few sharing points of different failure modes. A case study for a buried reinforced concrete structure has been conducted to show the applicability of the proposed damage assessment method.

2. Simplification of soil effect

The interaction between soil and structure is so complicated because of the complexity of the soil contents. During the physical process when a blast wave interacts with a buried structure, as shown in Fig. 1, the soil medium is considered as a macroscopical homogeneous material which can be simplified to an elastic foundation to support the structure. Therefore the soil-structure interaction (SSI) effect is simplified to a spring support which distributes over the structural element. The SSI effect exists in the deformation phase till the motion of element vanishes. Change of soil density during deformation is not considered; therefore the average stiffness of soil is adopted according to the analytical and laboratorial results (Sawangsurriya *et al.* 1974, Dutta *et al.* 2004). Such simplification aims on getting result efficiently in the analysis of the structure response by considering the SSI effect.

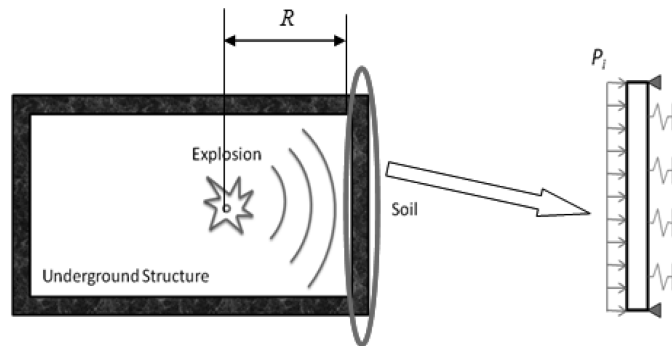


Fig. 1 Soil-structure interaction

3. Failure criteria

A typical resistance-deflection curve for laterally restrained elements is shown in Fig. 2 (TM5-1300, 1990). The initial portion of the curve is primarily due to the flexural action. The ultimate flexural resistance is maintained until 2 degrees of support rotation is produced. At this support rotation, the concrete begins to crush and the element loses flexural capacity. If adequate single leg stirrups were provided, the flexural action would be extended to 4 degrees. However, due to the presence of the continuous reinforcement and adequate lateral restraint, a tensile membrane action is developed. The resistance due to this action increases with increasing deflection up to incipient failure at approximately 12 degrees support rotation. In order to simplify the analysis, the resistance is assumed to be due to plastic action throughout the entire range of behavior. To approximate the energy absorbed under the actual resistance-deflection curve, the deflection of the idealized curve is limited to 8 degrees support rotation. Design for this maximum deflection would produce incipient failure conditions. Existing studies (Yu and Jones 1991, Krauthammer 1998) also suggested use the ratio of centerline-deflection to half-span as the criterion of bending failure, since the largest ductile plastic deformation usually appeared at the mid-span due to bending effects.

The maximum bending deformation of the element is defined as

$$y_m = L \cdot \tan \theta \tag{1}$$

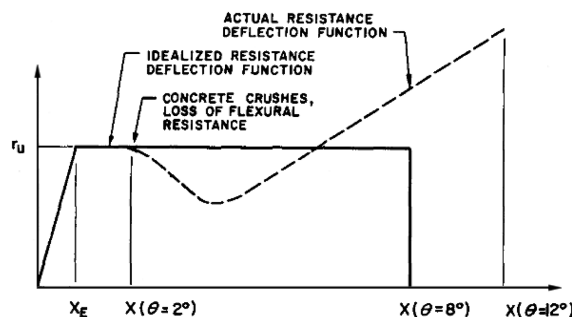


Fig. 2 Idealized resistance-deflection curve for large deflections

where L is half length of the element, and θ is the support rotation.

Since θ is small enough, $\tan\theta$ approximately equals to θ . Then y_m can be expressed as

$$y_m = L\beta \quad (2)$$

where β is the ratio of centerline deflection to half span.

For a reinforced concrete structure member, the dynamic bending strength M_0 varies for different cross section designs. According to TM5-1300, for type I design, there is no crushing or spalling in concrete; only cracking appears on the tension side and the M_0 can be expressed as

$$M_0 = \frac{A_s f_{ds}}{b} \left(d - \frac{a}{2} \right) \quad (3)$$

in which

$$a = \frac{A_s f_{ds}}{0.85 b f'_{dc}} \quad (4)$$

where A_s is the area of tension reinforcement within the width, f_{ds} is the dynamic design stress for reinforcement, b is the width of compression face, d is the distance from extreme compression fiber to centroid of tension reinforcement, a is the depth of equivalent rectangular stress block, f'_{dc} is the dynamic ultimate compressive strength of concrete.

In the cross section type II, cracking appears on the tension side of member while crushing appears on the compression side. The M_0 can be shown as

$$M_0 = \frac{A_s f_{ds} d_c}{b} \quad (5)$$

where A_s shows the area of tension or compression reinforcement within the width b , d_c is the distance between the centroids of the compression and the tension reinforcement.

In the cross section type III, disengagement of concrete appears on both tension and compression sides of the member. The bending strength M_0 is expressed the same as in Eq. (5).

The shear deformation at the element supports can be expressed by

$$y_s = \gamma_v \cdot \delta \cdot h \quad (6)$$

where y_s is cumulative quantity over of shear sliding, γ_v is the average shear strain, δ is a material parameter calculated from experiment result, h is the depth of the element. In the present study, δ is fixed as 0.8.

Therefore, the dynamic shear strength of a rectangular section reinforced concrete structure member, Q_0 can be expressed as

Table 1 Different damage level under empirical bending and shear failure criteria (Yu and Jones 1991)

Type of failure	Criteria	Light Damage (%)	Moderate Damage (%)	Severe Damage (%)
Shear	Average shear strain γ_v	1	2	3
Bending	Ratio of centerline deflection to half span β	3.492	8.749	14.054

$$Q_0 = 0.18f_{dc}'bd \quad (7)$$

Table 1 shows different damage level under empirical bending and shear failure criteria from results of Yu and Jones (1991) and Krauthammer (1998). There are three levels of damage, including light damage, moderate damage, and severe damage. For shear design, average shear strain γ_v indicates different damage levels, while the support rotation β is for bending.

4. Failure modes and response analysis

The internal blast load is simplified as a rectangular pulse load with magnitude of p_0 and duration of t_d , while the pulse shape effect is eliminated. The pulse shape effect has been discussed by Youngdahl (1970, 1971), Li and Meng (2002b), and Li and Jones (2005b) that the loading shape effects on the P-I diagrams of a rigid, perfectly plastic SDOF model can be eliminated by using the Youngdahl's correlation parameter method. For convenience of P-I equations derivation while not losing the generality of the solution, the rectangular pulse load with equivalent pressure and impulse is adopted in the present study. The pulse shape effects on the P-I diagrams of a rigid, perfectly plastic SDOF model can be eliminated by using the Youngdahl's (1971) correlation parameter method as follows.

$$\begin{cases} I = \int_{t_y}^{t_f} P(t)dt \\ t_{mean} = \frac{1}{I} \int_{t_y}^{t_f} (t-t_y)P(t)dt \\ P_e = \frac{I}{2t_{mean}} \end{cases} \quad (8)$$

where I is the impulse, t_y is the time when material begins to yield, t_f is the end time of total deformation, $P(t)$ is the external pressure, t_{mean} is the mean time, P_e is the effective pressure.

As discussed in section 2, the spring effect exists in all the phases. The governing equation is expressed as

$$\frac{\partial Q}{\partial x} = -p_0 + m\ddot{y} + Ky \quad (9)$$

where Q is the transverse shear force, x is the abscissa on the element, m is the mass per unit length, \ddot{y} is the acceleration of unit mass, K is equivalent spring coefficient to represent the SSI effect, and y is the displacement of unit mass. It is worth noting that the governing Eq. (9) considers the soil-structure interaction which has an additional term of the spring effect and is different from that derived for surface structures.

The same as the analysis of surface structure, there are totally five possible transverse velocity profiles including one pure shear failure mode, two pure bending failure modes, and two combined failure modes as shown in Fig. 3. A dimensionless strength ratio is introduced as below

$$v = \frac{Q_0L}{2M_0} \quad (10)$$

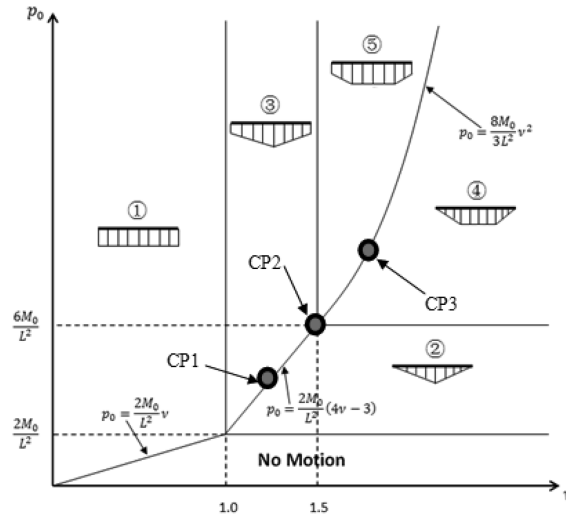


Fig. 3 Distribution of failure modes

Table 2 Velocity profile

	Mode 1	Mode 2	Mode 3	Mode 4	Mode 5
Phase 1					
Phase 2					
Phase 3	N.A.	N.A.			
Phase 4	N.A.	N.A.	N.A.	N.A.	

where Q_0 and M_0 are the dynamic shearing and bending strength respectively, L is the half length of the element.

Table 2 shows the velocity profile of different phases under different modes. Mode 1 contains shear failure only. Mode 2 is for simple bending failure which has a plastic hinge at the center of the element. Mode 3 can be considered as a combination of mode 1 and mode 2. Mode 4 is the complex bending failure mode which has a plastic zone at the middle of the element. And mode 5 is the combination of mode 1 and mode 4. Differentiation of the five failure modes is the same as that for surface structures. Detail discussion of the mode differentiation is given in Section 6. Derivation of the displacement time history for the five failure modes is summarized as follows. The x-axis starts at the mid of the beam and only half of a strip beam is considered due to symmetry as seen in Fig. 1.

Mode 1. $0 < v < 1$ and $p_0 \geq 2M_0 v/L^2$, shear failure mode.

This shear failure mode provides direct shear failure occurs at the two supports where carries the maximum shear force, while bending failure does not occur. In this mode, the dimensionless parameter v is less than one which indicates a very low shear-to-bending strength ratio.

There are totally two phases in this mode including a loading phase (phase 1) and a post-loading phase (phase 2) which end at t_d and t_f respectively.

In phase 1, the governing equation is

$$\frac{\partial Q}{\partial x} = -p_0 + m\ddot{y}_s + Ky_s \quad (11)$$

where \ddot{y}_s and y_s are the acceleration and displacement due to shear force respectively.

The boundary and initial conditions are

$$Q(x=0) = 0, \quad Q(x=L) = -Q_0 \quad (12)$$

$$\dot{y}_s(t=0) = 0, \quad y_s(t=0) = 0 \quad (13)$$

where \dot{y}_s is the velocity due to shear force.

Integrating Eq. (11) with respect to time, at the end of phase 1 when $t = t_d$, the maximum displacement and velocity of the element are shown as follows.

$$y_s(t_d) = \frac{(p_0L - Q_0)}{KL} \left[\cos\left(\frac{\sqrt{K}t_d}{\sqrt{m}}\right) - 1 \right] \quad (14)$$

$$\dot{y}_s(t_d) = \frac{(p_0L - Q_0)}{\sqrt{m}KL} \sin\left(\frac{\sqrt{K}t_d}{\sqrt{m}}\right) \quad (15)$$

In phase 2, the governing equation transfers to

$$\frac{\partial Q}{\partial x} = m\ddot{y}_s + Ky \quad (16)$$

Using Eq. (12) as the boundary conditions and Eqs. (14)-(15) as the initial conditions to solve Eq. (16), at the end of phase 2, the final time t_f will be

$$t_f = \arctan \left[\frac{\sin\left(\frac{\sqrt{K}t_d}{\sqrt{m}}\right)(p_0L - Q_0)}{p_0L + \frac{\sqrt{K}t_d}{\sqrt{m}} \cdot Q_0 - \cos\left(\frac{\sqrt{K}t_d}{\sqrt{m}}\right) \cdot p_0L} \right] + t_d \quad (17)$$

The element's final transverse displacement due to shear is

$$y_s(t_f) = \frac{\sqrt{m}}{\sqrt{K}} \sin(T_1) \cdot \dot{y}_s(t_d) + \cos(T_1) \cdot \frac{y_s(t_d) \cdot KL + Q_0}{KL} - \frac{Q_0}{KL} \quad (18)$$

where $T_1 = \sqrt{K}(t_f - t_d)/\sqrt{m}$.

Mode 2. $1 \leq \nu \leq 1.5$ and $2M_0/L^2 \leq p_0 \leq 2M_0(4\nu - 3)/L^2$, or $\nu \geq 1.5$ and $2M_0/L^2 \leq p_0 \leq 6M_0/L^2$, bending failure mode.

A bending failure mode will occur when the above conditions are satisfied. A plastic hinge is generated at the mid-span of the element. There are totally two phases in this mode including a

loading phase (phase 1) and a post-loading phase (phase 2) which end at t_d and t_f respectively.

In phase 1, the governing equation is

$$\frac{\partial Q}{\partial x} = -p_0 + m\ddot{y}_m \left(1 - \frac{x}{L}\right) + Ky_m \left(1 - \frac{x}{L}\right) \quad (19)$$

where \ddot{y}_m and y_m are the acceleration and displacement due to bending force respectively.

The boundary and the initial conditions are

$$Q(x=0) = 0, \quad Q(x=L) = -Q_0, \quad M(x=0) = M_0, \quad M(x=L) = 0 \quad (20)$$

$$\dot{y}_m(t=0) = 0, \quad y_m(t=0) = 0 \quad (21)$$

where \dot{y}_m is the velocity due to bending force.

Integrating Eq. (19), at the end of phase 1 when $t = t_d$, the maximum displacement and velocity of the element due to bending are shown respectively as follows.

$$y_m(t_d) = \frac{3(p_0L^2 - 2M_0)}{2KL^2} \left[1 - \cos\left(\frac{\sqrt{K}t_d}{\sqrt{m}}\right) \right] \quad (22)$$

$$\dot{y}_m(t_d) = \frac{3(p_0L^2 - 2M_0)}{2KL^2} \sin\left(\frac{\sqrt{K}t_d}{\sqrt{m}}\right) \quad (23)$$

In phase 2, the governing equation changes to

$$\frac{\partial Q}{\partial x} = m\ddot{y}_m \left(1 - \frac{x}{L}\right) + Ky_m \left(1 - \frac{x}{L}\right) \quad (24)$$

Using Eq. (20) as the boundary conditions and Eqs. (22)-(23) as the initial conditions, the final time t_f will be

$$t_f = \frac{\sqrt{m}}{\sqrt{K}} \cdot \arctan\left[\frac{\sqrt{m}KL^2 \cdot \dot{y}_m(t_d)}{KL^2 \cdot y_m(t_d) + 3M_0}\right] + t_d \quad (25)$$

The final bending displacement of the element is solved as

$$y_m(t_f) = \frac{\sqrt{m} \cdot \sin(T_1) \cdot \dot{y}_m(t_d)}{\sqrt{K}} + \frac{\cos(T_1)[KL^2 \cdot y_m(t_d) + 3M_0]}{KL^2} - \frac{3M_0}{KL^2} \quad (26)$$

Mode 3. $1 \leq \nu \leq 1.5$ and $p_0 > 2M_0(4\nu - 3)/L^2$, combined failure mode.

Mode 3 is the combination of mode 1 and mode 2. Both shear failure and bending failure occur to the element. The shear failure occurs at the two supports, while the bending failure induces plastic hinge at the mid-span of the element. There are three phases including one loading phase (phase 1) and two post-loading phases (phase 2 and phase 3) which end at t_d , t_s , and t_f respectively.

In phase 1, the governing equation is

$$\frac{\partial Q}{\partial x} = -p_0 + m\ddot{y}_s + m(\ddot{y}_m - \ddot{y}_s) \left(1 - \frac{x}{L}\right) + Ky_s + K(y_m - y_s) \left(1 - \frac{x}{L}\right) \quad (27)$$

with the same boundary and initial conditions given in Eqs. (20), (13), and (21).

Similar to mode 1 and mode 2, after integrating Eq. (27), at the end of phase 1 when $t = t_d$, the maximum displacement and velocity of the element due to shear and bending are given respectively as follows.

$$y_s(t_d) = \frac{\left[1 - \cos\left(\frac{\sqrt{K}t_d}{\sqrt{m}}\right)\right](p_0L^2 - 4Q_0L + 6M_0)}{KL^2} \quad (28)$$

$$\dot{y}_s(t_d) = \frac{\sin\left(\frac{\sqrt{K}t_d}{\sqrt{m}}\right) \cdot (p_0L^2 - 4Q_0L + 6M_0)}{\sqrt{m}KL^2} \quad (29)$$

$$y_m(t_d) = \frac{\left[1 - \cos\left(\frac{\sqrt{K}t_d}{\sqrt{m}}\right)\right](p_0L^2 + 2Q_0L - 6M_0)}{KL^2} \quad (30)$$

$$\dot{y}_m(t_d) = \frac{\sin\left(\frac{\sqrt{K}t_d}{\sqrt{m}}\right) \cdot (p_0L^2 + 2Q_0L - 6M_0)}{\sqrt{m}KL^2} \quad (31)$$

In phase 2, the governing equation is

$$\frac{\partial Q}{\partial x} = m\ddot{y}_s + m(\ddot{y}_m - \ddot{y}_s)\left(1 - \frac{x}{L}\right) + Ky_s + K(y_m - y_s)\left(1 - \frac{x}{L}\right) \quad (32)$$

The boundary conditions are still the same as in the first phase, while the velocities and displacements given in Eqs. (28)-(31) are used as the initial conditions. Solving Eq. (32), at the end of phase 2 when $t = t_s$, the displacement due to shear stops first, while the bending displacement remains to the next phase. The ending time t_s and the maximum displacement and velocity due to shear and bending are shown respectively as follows.

$$t_s = \frac{\sqrt{m}}{\sqrt{K}} \cdot \arctan\left[\frac{\sqrt{m}KL^2 \cdot \dot{y}_s(t_d)}{y_s(t_d) \cdot KL^2 + 4Q_0L - 6M_0}\right] + t_d \quad (33)$$

$$y_s(t_s) = \frac{\sqrt{m}KL^2 \dot{y}_s(t_d) \sin(T_2) + [KL^2 y_s(t_d) + 4Q_0L - 6M_0] \cos(T_2) - 4Q_0L + 6M_0}{KL^2} \quad (34)$$

$$y_m(t_s) = \frac{\sqrt{m}KL^2 \dot{y}_m(t_d) \sin(T_2) + [KL^2 y_m(t_d) - 2Q_0L + 6M_0] \cos(T_2) + 2Q_0L}{KL^2} \quad (35)$$

$$\dot{y}_m(t_s) = \frac{\sqrt{m}KL^2 \dot{y}_m(t_d) \sin(T_2) + [KL^2 y_m(t_d) - 2Q_0L + 6M_0] \sin(T_2)}{\sqrt{m}KL^2} \quad (36)$$

where $T_2 = \sqrt{K}(t_s - t_d)/\sqrt{m}$.

In phase 3, only the bending failure induced motion remains, and the governing equation is the same as Eq. (24). Similarly, the motion termination time t_f and the final displacement $y_m(t_f)$ are determined as

$$t_f = \frac{\sqrt{m}}{\sqrt{K}} \cdot \arctan \left[\frac{\sqrt{mKL^2} \cdot \dot{y}_m(t_s)}{KL^2 \cdot t_m(t_s) + 3M_0} \right] + t_s \quad (37)$$

$$y_m(t_f) = \frac{\sqrt{m}}{\sqrt{K}} \cdot \sin(T_3) \cdot \dot{y}_m(t_s) + \frac{[KL^2 \cdot y_m(t_s) + 3M_0] \cdot \cos(T_3)}{KL^2} - \frac{3M_0}{KL^2} \quad (38)$$

where $T_3 = \sqrt{K}(t_f - t_s)/\sqrt{m}$.

Mode 4. $1.5 < \nu$ and $p_0 > 8M_0 \nu^2/3L^2$, bending failure mode.

In this mode, the bending failure with a plateau deformation at the central portion of the element occurs when the blast load is sufficiently intensive. Different from mode 2, two plastic hinges are generated offset from the mid-span of the element. There are totally three phases including one loading phase (Phase 1) and two post-loading phases (phase 2 and phase 3) which end at t_d , t_1 , and t_f respectively.

In phase 1, the governing equation is expressed as

$$\frac{\partial Q}{\partial x} = -p_0 + m\ddot{y}_m \left(\frac{L-x}{L-\xi_0} \right) + Ky_m \left(\frac{L-x}{L-\xi_0} \right) \quad (39)$$

where ξ_0 is the distance of the plastic hinge from the mid-span.

The boundary conditions are as follows,

$$Q(x = \xi_0) = 0, \quad Q(x = L) = -Q_0, \quad M(x = \xi_0) = M_0, \quad M(x = L) = 0 \quad (40)$$

And the initial conditions are the same as Eqs. (13) and (21). Thus Eqs. (40), (13), and (21) are used to determine the integral constants when Eq. (39) is integrated.

At the end of the loading period, when $t = t_d$, the plastic hinge location which is indicated by ξ_0 and the ending displacement and velocity of phase 1 are derived respectively as follows.

$$\xi_0 = L - \frac{\sqrt{6p_0M_0}}{p_0} \quad (41)$$

$$y_m(t_d) = \frac{p_0 \left[1 - \cos \left(\frac{\sqrt{K}t_d}{\sqrt{m}} \right) \right]}{K} \quad (42)$$

$$\dot{y}_m(t_d) = \frac{p_0 \cdot \sin \left(\frac{\sqrt{K}t_d}{\sqrt{m}} \right)}{\sqrt{m}K} \quad (43)$$

In phase 2, the blast load has been released, and the velocity profile is the same as that given in phase 1. However, the two plastic hinges move toward the mid-span of the element. At the end of phase 2, the two plastic hinges meet at the mid-span and phase 3 motion starts then. The governing

equation of phase 2 is

$$\frac{\partial Q}{\partial x} = m\dot{y}_m \left(\frac{L-x}{L-\xi} \right) + Ky_m \left(\frac{L-x}{L-\xi} \right) \quad (44)$$

where ξ is the distance between the plastic hinge and the mid-span of the element.

The boundary conditions are

$$Q(x = \xi) = 0, \quad Q(x = L) = -Q_0, \quad M(x = \xi) = M_0, \quad M(x = L) = 0 \quad (45)$$

Using Eqs. (13) and (21) as the initial condition to solve Eq. (44). At the end of phase 2 when $t = t_1$, moving of the two plastic hinges stops. The ending time of phase 2 and the maximum displacement and velocity due to bending are shown respectively as follows,

$$t_1 = \frac{\ln\left(\frac{p_0 \cdot C + 6BM_0}{p_0}\right) \cdot A - \ln(C + BL^2) \cdot A}{2B} + t_d \quad (46)$$

where $A = 4Q_0(L - \xi_0) - 6M_0$, $B = y_s(t_d) \cdot K \cdot (L - \xi^2)^2$, $C = 6M_0 - 2Q_0(L - \xi_0)$

$$y_m(t_1) = \dot{y}_m(t_d) \cdot (t_1 - t_d) + y_m(t_d) \quad (47)$$

$$y_m(t_1) = \frac{p_0 \cdot \sin\left(\frac{\sqrt{K}t_d}{\sqrt{m}}\right)}{\sqrt{mK}} \quad (48)$$

In phase 3, the governing equation is the same as Eq. (24), and it can be solved in a similar way as it was done for mode 2 and mode 3.

At the end of phase 3, when $t = t_f$ the motion stops and the final time t_f is determined as

$$t_f = \frac{\sqrt{m}}{\sqrt{K}} \cdot \arctan\left[\frac{p_0 L^2 \cdot \sin(\sqrt{K}t_d/\sqrt{m})}{KL^2 \cdot y_m(t_1) + 3M_0}\right] + t_1 \quad (49)$$

The final bending displacement $y_m(t_f)$ is

$$y_m(t_f) = \frac{\sqrt{m}}{\sqrt{K}} \cdot \dot{y}_m(t_1) \cdot \sin(T_4) \cdot \frac{[KL^2 \cdot y_m(t_1) + 3M_0]}{KL^2} \cdot \cos(T_4) - \frac{3M_0}{KL^2} \quad (50)$$

where $T_4 = \sqrt{K}(t_f - t_1)/\sqrt{m}$.

Mode 5. $1.5 < \nu$ and $6M_0/L^2 \leq p_0 \leq 8M_0 \nu^2/3L^2$, combined failure mode.

Mode 5 is the most complicated mode as mode 1 and mode 4 are combined. There are four phases including one loading phase (phase 1) and three post-loading phases (phase 2, phase 3, and phase 4) which end at t_d , t_s , t_1 , and t_f respectively.

In phase 1, both shear and bending deformation occur. The governing equation is

$$\frac{\partial Q}{\partial x} = -p_0 + \dot{m}y_s + m(\dot{y}_m - \dot{y}_s) \left(\frac{L-x}{L-\xi_0} \right) + Ky_s + K(y_m - y_s) \left(\frac{L-x}{L-\xi_0} \right) \quad (51)$$

The boundary conditions are the same as those in Eq. (20), and initial conditions are the same as

Eqs. (13) and (21). After integrating Eq. (51), at the end of phase 1 when $t = t_d$, the plastic hinge location, the maximum displacement and velocity of this phase are shown respectively as follows.

$$\xi_0 = L - \frac{3M_0}{Q_0} \quad (52)$$

$$y_s(t_d) = \frac{\left[1 - \cos\left(\frac{\sqrt{K}t_d}{\sqrt{m}}\right)\right](3p_0M_0 + 2Q_0^2)}{3KM_0} \quad (53)$$

$$\dot{y}_s(t_d) = \frac{(3p_0M_0 - 2Q_0^2) \cdot \sin\left(\frac{\sqrt{K}t_d}{\sqrt{m}}\right)}{3\sqrt{m}KM_0} \quad (54)$$

$$y_m(t_d) = \frac{p_0 \left[1 - \cos\left(\frac{\sqrt{K}t_d}{\sqrt{m}}\right)\right]}{K} \quad (55)$$

$$\dot{y}_m(t_d) = \frac{p_0 \cdot \sin\left(\frac{\sqrt{K}t_d}{\sqrt{m}}\right)}{\sqrt{m}K} \quad (56)$$

In phase 2, the velocity profile is the same as that of the previous phase, while the shear deformation tends to vanish. The governing equation is

$$\frac{\partial Q}{\partial x} = \ddot{m}y_s + m(\ddot{y}_m - \ddot{y}_s)\left(\frac{L-x}{L-\xi_0}\right) + Ky_s + K(y_m - y_s)\left(\frac{L-x}{L-\xi_0}\right) \quad (57)$$

Based on the same boundary conditions given in Eq. (19), and the initial conditions of Eqs. (53)-(56), Eq. (57) can be integrated with respect to time. At the end of phase 2 when $t = t_s$, the shear deformation stops. The displacement and velocity at the ending time of phase 2 due to shear and bending are shown respectively as follows,

$$t_s = \frac{\sqrt{m}}{\sqrt{K}} \cdot \arctan \frac{\dot{y}_s(t_d) \cdot \sqrt{m}K(L-\xi_0)^2}{4Q_0(L-\xi_0) - 6M_0 + y_s(t_d) \cdot K \cdot (L-\xi_0)^2} \quad (58)$$

$$y_s(t_s) = \frac{\sqrt{m}}{\sqrt{K}} \dot{y}_s(t_d) \cdot \sin(T_2) + \frac{\cos(T_2) \cdot (A+B)}{K(L-\xi_0)^2} - \frac{A}{K(L-\xi_0)^2} \quad (59)$$

$$y_m(t_s) = \frac{\sqrt{m}}{\sqrt{K}} \dot{y}_s(t_d) \cdot \sin(T_2) + \frac{\cos(T_2)(C+B)}{K(L-\xi_0)^2} - \frac{C}{K(L-\xi_0)^2} \quad (60)$$

$$\dot{y}_m(t_s) = \dot{y}_m(t_d) \quad (61)$$

In phase 3, the bending deformation remains the same velocity profile as that in phase 2 of mode 4, and the two plastic hinges start to move toward the mid-span of the element. The governing

equation is the same as Eq. (44). Similarly, at the end of phase 3, when $t = t_1$, the two plastic hinges coincides at the mid-span, and the ending displacement and velocity of phase 3 are deduced as follows.

$$t_1 = \frac{\ln\left(\frac{p_0 F + 6EM_0}{P_0}\right) \cdot D - \ln(F + EL^2) \cdot D}{2E} + t_d \quad (62)$$

where $D = p_0 \sqrt{m} \cdot \sin(\sqrt{K} t_d / \sqrt{m}) / \sqrt{K}$, $E = p_0 [\cos(\sqrt{K} t_d / \sqrt{m}) - 1]$, $F = -3M$.

$$y_m(t_1) = \dot{y}_m(t_1) \cdot (t_1 - t_s) + y_m(t_s) \quad (63)$$

$$\dot{y}_m(t_1) = \dot{y}_m(t_s) \quad (64)$$

Similarly, in phase 4 of mode 5, the governing equation is the same as Eq. (24). At the end of phase 4 when $t = t_f$, the motion stops.

$$t_f = \frac{\sqrt{m}}{\sqrt{K}} \cdot \arctan\left[\frac{p_0 L^2 \cdot \sin(\sqrt{K} t_d / \sqrt{m})}{KL^2 \cdot y_m(t_1) + 3M_0}\right] + t_1 \quad (65)$$

The final bending displacement is

$$y_m(t_f) = \frac{\sqrt{m}}{\sqrt{K}} \cdot \dot{y}_n(t_1) \cdot \sin(T_4) + \frac{[KL^2 \cdot y_m(t_1) + 3M_0]}{KL^2} \cdot \cos(T_4) - \frac{3M_0}{KL^2} \quad (66)$$

5. P-I diagrams and discussions

In each of the five modes discussed in section 4, the final shear displacement y_s for direct shear failure and the final bending displacement y_m for bending failure, or both for combined failure can be derived. Based on the failure criteria discussed in section 3, P-I diagrams for different modes can then be derived.

Define dimensionless variables P^* and I^* of the pressure and impulse of a blast load as:

$$P^* = \frac{p_0 L^2}{M_0} \quad (67)$$

$$I^* = \frac{\sqrt{K} t_d P^*}{\sqrt{m} L} \quad (68)$$

From the equations for final displacements induced by shear and bending failure, the P-I diagrams can be represented in unified forms as follows.

$$S(P^*, I^*) = \delta \cdot h \cdot \gamma_v = y_s \quad (69)$$

$$\beta(P^*, I^*) = L \cdot \beta = y_m \quad (70)$$

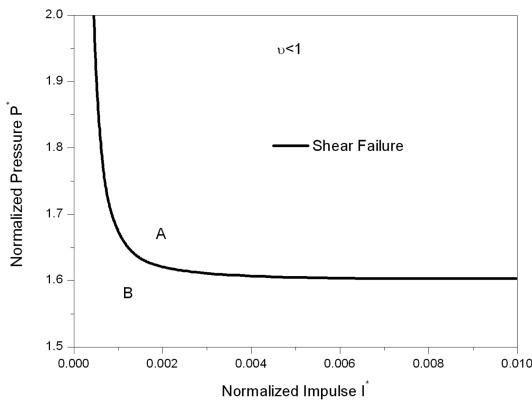
where y_s is the maximum displacement due to shear which equals to $y_s(t_f)$ in a shear failure mode,

and $y_s(t_s)$ in a combined failure mode; y_m is the maximum displacement due to bending which equals to $y_m(t_f)$; $S(P^*, I^*)$ and $B(P^*, I^*)$ are implicit expressions with respect to the normalized pressure and impulse for shear and bending according to failure criteria respectively. $S(P^*, I^*)$ equals to the right part of Eqs. (18), (34), or (59) which gave the maximum shear deformation, and $B(P^*, I^*)$ equals to the right part of Eqs. (26), (38), (50), or (66) which represent the maximum bending deformation.

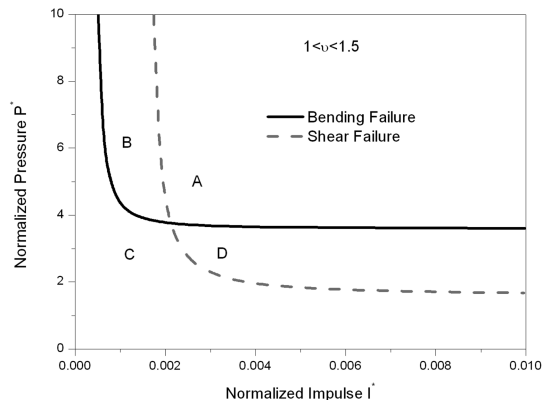
Based on Eqs. (69) and (70), P-I diagrams corresponding to shear and bending failures can be drawn.

5.1 Differentiation of failure modes

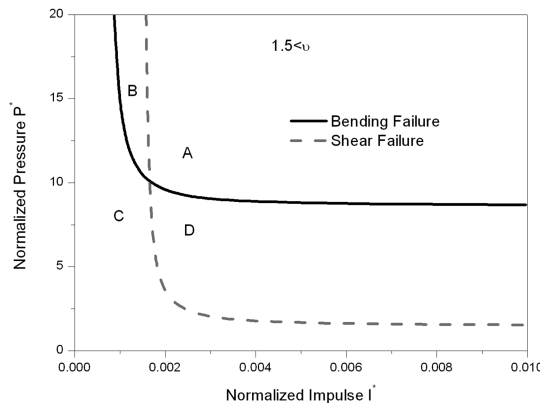
By determining relative parameters, the P-I diagrams can be plotted for all five failure modes. Differentiation of the failure modes given in Fig. 3 is determined by the requirement of the motion initiation. For example, for mode 1, the acceleration induced by the shear force at the supports should be larger than zero, and the maximum bending moment should be smaller than the bending strength of the element. Therefore $p_0 \geq 2M_0 \nu / L^2$ and $0 < \nu < 1$ are derived, respectively. For mode



(a) Typical failure mode $\nu \leq 1.0$ (Mode 1)



(b) Typical failure mode $1 \leq \nu \leq 1.5$ (Mode 3)



(c) Typical failure mode $1.5 \leq \nu$ (Mode 5)

Fig. 4 Typical failure modes

2, the initial acceleration due to bending should be larger than zero, while the maximum shear force should be less than the shear strength. Therefore $1 \leq \nu \leq 1.5$ and $2M_0/L^2 \leq p_0 \leq 2M_0(4\nu - 3)/L^2$, or $\nu \geq 1.5$ and $2M_0/L^2 \leq p_0 \leq 6M_0/L^2$ are required. For mode 3, by combining the two requirements that accelerations due to both shear and bending are larger than zero, the equations of boundaries are derived as $1 \leq \nu \leq 1.5$ and $p_0 > 2M_0(4\nu - 3)/L^2$. The mode 4 has the same requirements as mode 2 and the boundaries are $1.5 < \nu$ and $p_0 > 8M_0\nu^2/3L^2$. The mode 5 has the same requirements as mode 3, and the boundaries are $1.5 < \nu$ and $6M_0/L^2 \leq p_0 \leq 8M_0\nu^2/3L^2$.

Three typical P-I diagrams of shear and bending failures are plotted in Fig. 4.

- 1) When $\nu = 0.8$ and $p_0 > 8M_0\nu/L^2$, only shear failure exists as shown in Fig. 4(a) (mode 1). Region A and region B indicate shear failure and no failure respectively.
- 2) As shown in Fig. 4(b) when $\nu = 1.2$ and $p_0 > 2M_0(4\nu - 3)/L^2$, the element fails in the mode 3, which is the combination of mode 1 and mode 2. Two P-I diagrams, for shear failure and bending failure respectively, are plotted based on Eqs. (69)-(70). There are four regions in this case which indicate four different failure types of the element. In region A, which corresponds to larger pressure and impulse, combined failure occurs since both the maximum shear displacement and the maximum bending displacement exceed the failure threshold given by the shear and bending failure criteria. In region B, the pair of pressure and impulse locates above the shear failure diagram but below the bending failure diagram, which indicates shear failure only occurred to the element. Similarly, in region D, the pair of pressure and impulse exceeds the bending failure diagram while it is below the shear failure diagram, which defines bending failure for the element. In region C, the element remains safe due to the pressure and impulse pair is below both diagrams.
- 3) When $\nu = 1.8$ and $p_0 > 6M_0\nu^2/L^2$, mode 4 and mode 5 may occur. Fig. 4(c) shows the P-I diagrams of mode 5 which is similar to mode 2 with 4 different regions.

5.2 Soil-structure interaction effect

The boundary conditions of different failure modes are exactly the same as those of surface structures. This is because that, whether the spring effect acts on the beam or not, the initial

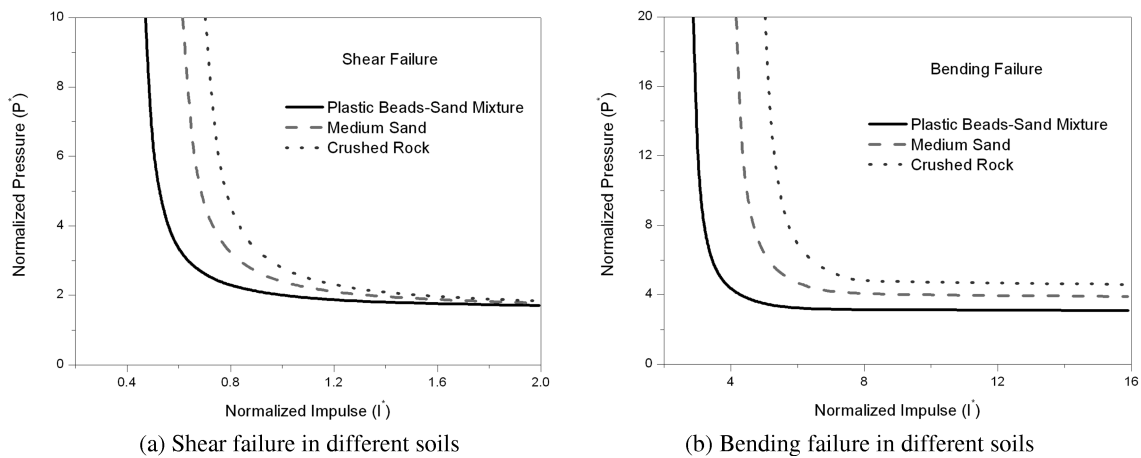


Fig. 5 Failures in different soils

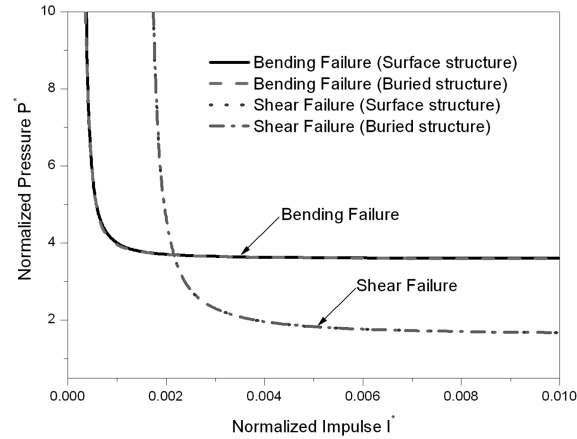


Fig. 6 Comparison with surface structures under blast load

conditions for all the failure modes remain the same.

Different soil has different density and compressibility, therefore the spring effect varies in all kinds of soil types. Considering a comparison with plastic beads-sand mixture ($K = 2.39$ MN/m), medium sands ($K = 3.83$ MN/m), and Crushed rock ($K = 4.83$ MN/m) (Sawangsurriya *et al.* 1974), P-I diagrams for shear and bending failure are plotted and compared in Fig. 5. It shows that, these three types of soil are characterized as low stiffness, intermediate stiffness, and high stiffness. The low stiffness material is a mixture of 50% by volume of sand and 50% by volume of plastic beads. The intermediate stiffness material is a medium of uniformly-graded quartz sand. The high stiffness material is 19-mm crushed lime rock. It can be seen from Fig. 5. that, the crushed rock has the highest stiffness and has significant effect on the structural failure.

Comparison is also done to the damage assessment results for surface structures when the spring coefficient is set sufficient small (for example, $K = 10$ N/m) as shown in Fig. 6. It can be seen that both the shear failure and bending failure diagrams match well with those for surface structures. It verifies the present P-I diagrams and the P-I diagram method suggested by Ma *et al.* (2007) has been successfully extended to damage assessment for buried structures when the decoupling of SSI is considered. Furthermore, the present results can be applied to damage assessment for surface structures by assigning a sufficient small spring coefficient in the equations.

5.3 Verification of continuity

Since different failure modes give different final shear and/or bending displacement, the solutions at the boundaries of different modes in Fig. 3 should be continuous. It means that two modes should give the same P-I diagram at their sharing boundary line. To verify the continuity of the equations, three checking points as shown in Fig. 3 are examined. CP1 ($p_0 = 3.6M_0/L^2$ and $\nu = 1.2$) is shared by mode 2 and mode 3, CP2 ($p_0 = 6M_0/L^2$ and $\nu = 1.5$) is shared by mode 2, mode 3, mode 4 and mode 5, and CP3 ($p_0 = 8.64M_0/L^2$ and $\nu = 1.8$) is shared by mode 4 and mode 5. CP1 and CP3 are chosen randomly from the boundary lines.

The verification is shown in Table 3 which indicates the diagrams of Mode 2, 3, 4, and 5 match very well at the check points.

Table 3 Continuity verification

Mode	$\nu = 1.2$		$\nu = 1.5$		$\nu = 1.8$	
	P^*	I^*	P^*	I^*	P^*	I^*
2	3.6	0.3883	6.0	0.3169	N.A.	N.A.
3	3.6	0.3883	6.0	0.3169	N.A.	N.A.
4	N.A.	N.A.	6.0	0.3169	8.4	0.3032
5	N.A.	N.A.	6.0	0.3169	8.4	0.3032

6. Case study

To verify the applicability of the developed P-I diagrams, a case study is carried out by considering a box-shape buried structure. An explosion occurred inside the buried structure as schematically shown in Fig. 1. Damage assessment for the side wall is carried out and one unit strip of side wall is considered for simplicity. The soil layer is medium sands and relative parameters are given below.

Half element length: $L = 2$ m

Element height: $h = 0.2$ m

Unit mass of element: $m = 500$ kg/m²

Shear resistance of element: $Q_0 = 252.8$ kN

Bending resistance of element: $M_0 = 153.3$ kN·m

Soil spring coefficient: $K = 3.83$ MN/m

Charge weight: $W = 125$ kg

Once the distance R is confirmed, using the above parameters, the constant pressure p_0 and blast duration t_d can be approximated by using relative equations or read from charts. Subsequently, the normalized pressure and impulse are calculated. In the present case study, three different distances $R = 12.7$ m, 14.0 m and 15.6 m, are considered respectively (see Table 4).

ν is calculated as 1.374, the failure criteria of Eqs. (69) and (70) in which $\beta = 3.492\%$ and $\gamma_v = 1\%$ are used for light damage criteria. Judging from Fig. 3, the failure mode is Mode 5, which is the most complex combination of shear and bending failures. As shown in Fig. 7, point Z1 is in region A, point Z2 is in region B, and point Z3 is in region C. That means, when the scaled distance is 1.674, the structure will endure both light shear and light bending damage; when the scaled distance is 2.045, the structure will endure light bending damage only; when the scaled distance is 2.760, the structure is safe.

Table 4 Case study

Point	Distance (R)	Duration (t_d)	Scaled Distance (Z)	Normalized Impulse (I^*)	Pressure (p_0)	Normalized Pressure (P^*)
Z1	12.7 m	2.535 ms	1.674 m/kg ^{1/3}	5.271	1.086 MPa	33.95
Z2	14.0 m	2.797 ms	2.045 m/kg ^{1/3}	3.246	0.606 MPa	18.95
Z3	15.6 m	3.117 ms	2.760 m/kg ^{1/3}	1.591	0.276 MPa	8.338

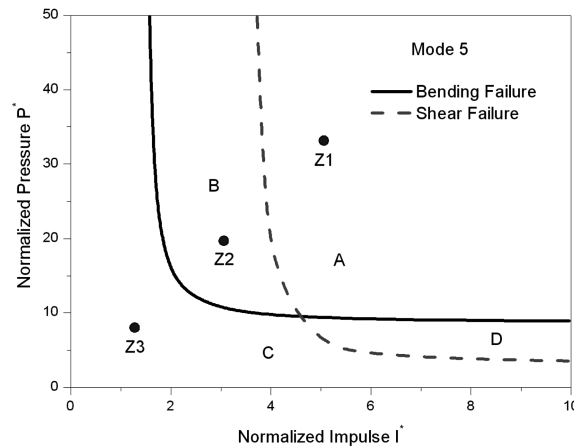


Fig. 7 Case study

7. Conclusions

The present study derives P-I diagrams for underground buried structures subjected to internal blast load. The soil-structure interaction is considered and a rigid-plastic beam model is applied in order to consider the combined effect of both shear and bending failure. Verification shows that the present analysis is a successful extension of damage assessment of surface structures to buried structures. Results show that with increase of the soil stiffness, the soil-structural interaction and its effect to the structural damage becomes very significant.

An internal detonation generates very complicated blast load to the buried structure walls, ceiling and floor, which is affected by many factors, such as venting, geometry of the buried structure, charge weight and the way of charge placement, etc. In the present study, the distance from centroid of charge to the beam element changes along the beam. For example, when the charge is placed at the floor of the buried structure, the maximum distance will be $\sqrt{4L^2 + R^2}$, where R is the perpendicular distance from centroid of charge to the beam element. Therefore the scaled distance is sensitive to the ratio of L/R . To ensure the difference of the peak pressure along the beam within 10%, L/R should be less than 0.229. Under the above considerations, the present study assumed that the blast load is uniformly acted to the structural element which gives a conservative assessment of structural damage and leads to a safer design for underground protective structures. And the localized damage due to unevenly distributed blast load is not in the scope of the present study.

The structural element in analysis is simplified to a simply-supported beam model which ignores the rigidity at the supports. This again results in conservative assessment of structural damage and gives a safe design of the structure although adjustment of the P-I diagrams can be done for a fixed beam as it has been done for surface structures (Ma *et al.* 2007).

The rigid-plastic model ignores the elastic deformation stage which may cause discrepancies at the minor damage case, however, it can well represent the structural deformation behavior when the structure undergoes mediate and large deformations.

In the present analysis, a rectangular pulse shape is adopted. The pulse shape effect to the P-I diagrams is minor especially in the two extreme impulsive and quasi-static cases.

Besides, the rate dependence of the soil stiffness is also not considered in the analysis which is

mainly due to that experimental data on the soil stiffness rate dependence is not available.

References

- Alves, M. and Jones, N. (2002), "Impact failure of beams using damage mechanics: Part I - Analytical model", *Int. J. Impact Eng.*, **27**(8), 837-861.
- Campidelli, M. and Viola, E. (2007), "An analytical-numerical method to analyze single degree of freedom models under airblast loading", *J. Sound Vib.*, **302**, 260-286.
- Dutta, S., Mandal, A. and Dutta, S.C. (2004), "Soil-structure interaction in dynamic behaviour of elevated tanks with alternate frame staging configurations", *J. Sound Vib.*, **277**, 825-853.
- Fallah, A.S. and Louca, L.A. (2007), "Pressure-impulse diagrams for elastic-plastic-hardening and softening single-degree-of-freedom models subjected to blast loading", *Int. J. Impact Eng.*, **34**(4), 823-842.
- Jones, N. (1989), "On the dynamic inelastic failure of beams", In: Wierzbicki, T. and Jones, N. editors, *Structural Failure*, New York: Wiley, 133-159.
- Jones, N. (1997), "Structural impact, Paperback Ed. Cambridge", *Cambridge University Press*.
- Jones, N. and Jones, C. (2002), "Inelastic failure of fully clamped beams and circular plates under impact loading", *Proceedings of the Institution of Mechanical Engineers. Part C. J. Mech. Eng. Sci.*, **216**(2), 133-149.
- Jones, N. and Song, B. (1986), "Shear and bending response of a rigid plastic beam to partly distributed blast type loading", *Mech. Based Des. Struct. Mach.*, **14**(3), 275-320.
- Kalthoff, J.F. and Winkler, S. (1987), "Failure mode transition at high rates of loading", In: Chiem, C.Y. et al., editors. *Proceedings of the International Conference on Impact Loading and Dynamic Behaviour of Materials*, Bremen, Deutsche Gesellschaft für Metallkunde, DGM, 185-196.
- Kalthoff, J.F. (1990), "Transition in the failure behavior of dynamically shear loaded cracks", In: Chen, C.F., Kunze, H.D. and Meyer, L.W. editors. *Proceedings of the 11th US National Conference of Applied Mechanics*, Arizona: TUCSON, May, 5247-5250.
- Krauthammer, T. (1998), "Blast mitigation technologies: developments and numerical considerations for behavior assessment and design", *Proceedings of international conference on structures under shock and impact*, SUSI, Melbourne, Australia 1-10.
- Krauthammer, T., M. ASCE, Bazeos, N., and Holmquist, T.J. (1986), "Modified SDOF analysis of RC box-type structures", *J. Struct. Eng.*, **112**(4), 726-744.
- Lellep, J. and Torn, K. (2005), "Shear and bending response of a rigid-plastic beam subjected to impulsive loading", *Int. J. Impact Eng.*, **31**(9), 1081-1105.
- Li, Q.M. and Jones, N. (1999), "Shear and adiabatic shear failures in an impulsively loaded fully clamped beam", *Int. J. Impact Eng.*, **22**, 589-607.
- Li, Q.M. and Meng, H. (2002a), "Pressure-impulse diagram for blast loads based on dimensional analysis and single-degree-of-freedom model", *J. Eng. Mech.*, **128**(1), 87-92.
- Li, Q.M. and Meng, H. (2002b), "Pulse loading shape effects on pressure-impulse diagram of an elastic-plastic, single-degree-of-freedom structural model", *Int. J. Mech. Sci.*, **44**, 1985-1998.
- Li, Q.M. and Jones, N. (2005a), "Shear and adiabatic shear failures in an impulsively loaded fully clamped beam", *Int. J. Impact Eng.*, **31**(7), 877-893.
- Li, Q.M. and Jones, N. (2005b), "Foundation of correlation parameters for eliminating pulse shape effects on dynamic plastic response of structures", *J. Appl. Mech.*, **72**(2), 172-176.
- Liu, J.H. and Jones, N. (1988), "Dynamic response of a rigid plastic clamped beam struck by a mass at any point on the span", *Int. J. Solids Struct.*, **24**, 251-270.
- Ma, G.W., Shi, H.J. and Shu, D.W. (2007), "P-I diagram method for combined failure modes of rigid-plastic beams", *Int. J. Impact Eng.*, **34**, 1081-1094.
- Martin, J.B. and Symonds, P.S. (1966), "Mode approximation for impulsively loaded rigid plastic structures", *J. Eng. Mech. Div.*, **92**(EM5), 43-66.
- Menkes, S.B. and Opat, H.J. (1973), "Broken beams", *Exp. Mech.*, **13**, 480-486.
- Sawangsurriya, A., Bosscher, P.J., and Edil, T.B. (1974), "Laboratory evaluation of the soil stiffness gauge (SSG)", *Transportation Research Record ISSN 0361 - 1981 CODEN TRREDM*, 30-37.

- Smith, P.D. and Hetherington J.G. (1994), *Blast and Ballistic Loading of Structures*, Oxford: Butterworth-Heinemann.
- Symonds, P.S. (1968), "Plastic shear deformation in dynamic load problems", In: Heyman, J. and Leckie, F.A. editors. *Engng plasticity*. Cambridge: *Cambridge University Press.*, 647-664.
- Symonds, P.S. and Chon, C.T. (1979), "Large visco plastic deflections of impulsively loaded plane frames", *Int. J. Solids Struct.*, **15**(1), 15-31.
- TM5-1300 (1990), "Structures to resist the effects of the accidental explosions", US Department of Army, New Jersey.
- Youngdahl, C.K. (1970), "Correlation parameters for eliminating the effect of pulse shape on dynamic plastic deformation", *J. Appl. Mech.*, ASME, **37**, 744-752.
- Youngdahl, C.K. (1971), "Influence of pulse shape on the final plastic deformation of a circular plate", *Int. J. Solids Struct.*, **7**, 1127-1142.
- Yu, J.L. and Jones, N. (1991), "Further experiment investigations on the failure of clamped beams under impact loads", *Int. J. Solids Struct.*, **27**, 1113-1137.